Contents lists available at ScienceDirect

Applied Materials Today

journal homepage: http://ees.elsevier.com

Journal Cover Image

# The causal relationship between melt pool geometry and energy absorption measured in real time during laser-based manufacturing

Brian J. Simonds [a,*], Jack Tanner [a], Alexandra Artusio-Glimpse [a], Paul A. Williams [a], Niranjan Parab [b], Cang Zhao [b,c], Tao Sun [b,d]

[a] Applied Physics Division, Physical Measurements Laboratory, National Institute of Standards and Technology, Boulder, CO 80305, United States
[b] X-ray Science Division, Advanced Photon Source, Argonne National Laboratory, Lemont, IL 60439, United States
[c] Department of Mechanical Engineering, Tsinghua University, Beijing, China
[d] Department of Materials Science and Engineering, University of Virginia, Charlottesville, VA, United States



ARTICLE INFO

*Article history:*
Received 31 December 2020
Received in revised form 1 April 2021
Accepted 21 April 2021
Available online xxx

ABSTRACT

During laser powder bed fusion additive manufacturing, laser power absorption is governed by a protean pool of molten metal that can present as a highly reflective surface, a deeply absorbing cavity, or some amalgamation thereof. These melt pool dynamics have been linked to defect creation, porosity, and surface finish quality. Although these are therefore critical for determining final part quality, their instantaneous influence on laser absorption have only been explored through simulation. To date, direct real-time observations have been elusive due to the locally extreme environment. In this work, we focus a laser on Ti-6Al-4V powder and bare plate while quantifying the time-dependent, absolute energy absorption by monitoring omnidirectional backscattered laser intensity. We also simultaneously record the projective melt pool geometries with high-speed synchrotron x-ray imaging. We find that laser absorption strongly reflects the stability of the vapor depression over a wide range of applied laser powers, oxygen content in the processing atmosphere, and with the presence of powder. During laser scanning of a powder bed surface, we find a significant absorption reduction after 400 μs due to a dramatic change in the vapor depression aspect ratio – an event known to create porosity. As several industrial scan strategies necessitate thousands of these events during a build, their identification and control is of significant practical importance. Lastly, a normalized enthalpy model is demonstrated to be effective in quantifying the relationship between the laser absorption and cavity depth, even under transient conditions. In addition to providing vital quantitative data for simulation calibration, the correlation of melt pool geometry with laser absorption during realistic processing conditions suggests the use of a total backscattered light detection system for real-time process control.



## 1. Introduction

Cavity-enhanced optical absorption is a well-studied phenomenon where a greater percentage of light can be absorbed by a cavity structure compared to a plane surface of the same material [1]. This is true irrespective of the material forming the cavity as it is a geometrical consequence whereby the cavity creates multiple absorption events for the internally scattered light. This phenomenon has been exploited for increased radiant emission from conical cavities [2,3] and for maximizing absorption in developing absolute radiometric calorimeters [4]. During laser-metal processing, cavities can form in the metal melt pool that similarly affect the incident laser beam. As laser welding and drilling was developed over 50 years ago, it was quickly understood that the extraordinarily deep melt penetration and high energy efficiency was owed to the enhanced absorption from a molten metal cavity [5]. More recently, in laser powder bed fusion (LPBF) additive manufacturing (AM), where a focused laser is used to selectively melt layers of metal powder to build complex 3-dimensional shapes, cavities have been found to play a major role as well [6,7]. Early analytical models of these processes calculated the effects of simple cavity geometries on laser absorption under idealized conditions [8–10]. More recent simulations incorporate more complicated cavity shapes generated by simulated fluid dynamics [11,12] or from experimental data [13].

In laser-metal processing, these cavities are generally referred to as vapor depressions due to the physics of their formation. Intense irradiation of a metal surface creates a boiling, molten pool that is depressed below its initial surface height due to a vaporization-induced recoil force. This is counteracted by a surface tension pressure that seeks to minimize surface energy by closing the opening. At relatively high irradiances ($> 1$ MW/cm$^2$), these vapor depressions can be especially deep and narrow that are colloquially referred to as keyholes. LPBF AM typi-

* Corresponding author.

https://doi.org/10.1016/j.apmt.2021.101049
2352-9407/

cally uses lower irradiances, which although form vapor depressions do not necessarily develop into a deep keyhole [7]. As a result of the innate relationship between laser power absorption and cavity shape, the stability of the vapor depression is critically important.

The tug-of-war between primarily vaporization and surface tension induced forces means that the cavities are inherently metastable. For LPBF AM, even constant processing conditions (laser power, scan speed, etc.) do not guarantee stability as scan strategies and powder bed variations can locally affect cavity behavior. Vapor depression instability can produce mechanically deleterious porosity that results from stochastic events where gas bubbles are trapped by a fast-moving solidification front in the wake of the scanned laser. Pore forming dynamics investigated through simulation [12,14] reveal the intimate relationship between laser absorption and cavity geometry. In general, as a keyhole grows deeper, laser energy absorption is highest at the bottom. For a melt with negative temperature-dependent surface tension coefficient [15], the resulting local rise in temperature increases the local recoil pressure and reduces the surface tension. Meanwhile, the steep sidewalls above the keyhole bottom are cooler because the laser light is mostly deflected deeper. Consequently, this region experiences a relative increase in surface tension that overcomes the recoil force [14]. Together, these events create a situation where the cavity pinches off the keyhole opening and traps vapor at the bottom. Furthermore, during these events the incoming laser absorption is reduced as it is momentarily incident to a smaller cavity [16]. This entire pore-formation process occurs on the scale of microseconds or less, depending on processing conditions.

Direct observation of the vapor depression geometry is becoming commonplace due to recent advancements using high-speed synchrotron x-ray imaging [7,17,18]. By employing high-flux, high-energy sources, x-ray imaging can reveal the laser-induced keyhole dynamics with high temporal and spatial resolutions. Time-resolved absorption measurements, on the other hand, are possible by measuring the total backscattered light during laser processing, typically with an integrating sphere [19,20], and performing an energy balance calculation to determine the amount of laser light absorbed by the material during processing. Recently, integrating sphere radiometry (ISR) has been developed as a metrology instrument for dynamic, absolute laser light coupling during intense laser irradiation of solid metals [21] and metal powders [22]. In this work, these two techniques are combined to provide unique, simultaneous measurements of laser absorption and keyhole cross-section so that the causal relationship between them can be experimentally quantified. So far, this relationship had been limited to multiphysics simulations [11,13,23,24] and thus another goal of this research is to provide first-of-their-kind data to calibrate and refine these simulations. In addition, the differences between absorption and cavity dynamics in bare metal plate versus metal powders are explored as this is of interest to both the AM and laser welding communities. Furthermore, this work reveals that measurements of total, relative backscattered light alone can detect cavity instabilities known to result in defects in as-built parts.

In order to improve the repeatability and reliability of laser-based AM, one needs a real-time, in situ process monitor capable of detecting the generation of defects and also informing process control on-the-fly. In situ monitoring is an active area of research in the field of AM and yet no clear preferential monitoring technique has emerged [25–27]. Imaging techniques, whether they be visual [28], thermal [29], or x-ray [30] have been demonstrated to be useful for monitoring keyhole instabilities and have been correlated with porosity [31]. However, these techniques require a significant amount of instrumentation and data processing making them ill-suited for large-scale deployment. Lower dimension monitoring techniques such as ultrasound [32], photodiodes [33], pyrometry [34], and spectroscopy [35,36] have also been used for defect detection. Although data collected using these sensors are more readily processed, their use to detect defect creation events is typically only correlative and requires additional calibration by complimentary techniques.

As an alternative, total backscattered laser light detection is appealing for real-world implementation for several reasons. First, it necessitates only a single photodiode and is therefore capable of high time resolution (sub-nanosecond) at low cost while producing a computationally preferred one-dimensional data stream. Second, unlike previous photodiode-based monitoring systems that measure scattered light over a small solid angle, an integrating sphere approach ensures that virtually all scattered light is collected. As will be demonstrated here, this feature enables the causal relationship between cavity geometry and laser absorption to be established. Third, calibration of the signal allows for the absolute determination of absorbed laser power in real-time [21]. Although not necessary for defect detection, this ability leads to a greater connection between industrial process parameters and predictive models that need to know the amount of absorbed energy. This is a stated goal for "Industry 4.0" [37], which seeks to digitize the entire manufacturing process by, for instance, creating a "digital twin" [38]. Lastly, total backscattered light detection could be readily deployed since LPBF AM build chambers could themselves become a light integrating apparatus as demonstrated in a custom built, metrology-grade AM system [56].

## 2. Materials and methods

### 2.1. Metal samples

The Ti-6Al-4V plate samples were machined out of NIST Standard Reference Material 654b [39] using wire electric discharge machining. These were thinned to approximately 300 μm by polishing of the sides to which the x-rays were incident. This thickness was necessary for adequate x-ray transmission at the high frame rate (50,000 frames per second) x-ray imaging used here. The polished sides also created a highly specular surface which is necessary for good contrast of keyhole and melt pool in the x-ray images. The laser incident surface was also polished to a specular finish. For measurements involving powder, the Ti-6Al-4V sample was sandwiched between two glassy carbon plates (1 mm thickness). The difference in height between these plates and the metal substrate surface created a trough into which powder was spread. The Ti-6Al-4V powder (Goodfellow Corporation, US, Grade 23 [40]) was gas-atomized (good sphericity) and had a maximum particle size of 45 μm.

### 2.2. Integrating sphere radiometry

The integrating sphere technique is generally the same as that used in Ref. [21]. In brief, a calibrated integrating sphere was placed over the sample to collect the backscattered laser light. The amount of absorbed laser power is then determined from an energy balance calculation between the measured input and scattered laser light (zero light transmission). The sphere used in these measurements had an elongated inlet aperture at the top to allow for a scanned process laser. A small channel along the sphere base accommodated clear passage of the 2 mm wide x-ray beam. Fig. 1 shows a diagram of the integrating sphere apparatus as it was implemented with the x-ray beam. The laser had an angle of incidence of 7° relative to the sample surface normal. This ensured that the strong backscattered light from the initially specular surface would be captured within the sphere. The backscattered light was measured by a photodiode that was fiber-coupled to the sphere surface; it was bandpass filtered at 1070 nm. The photodiode voltage was measured by a high-speed oscilloscope with a 1 % voltage uncertainty and a 40 ns time resolution. A calibration procedure using a well-characterized scattering surface in place of the experimental target produces a coefficient that converts the photodiode signal to an ab-

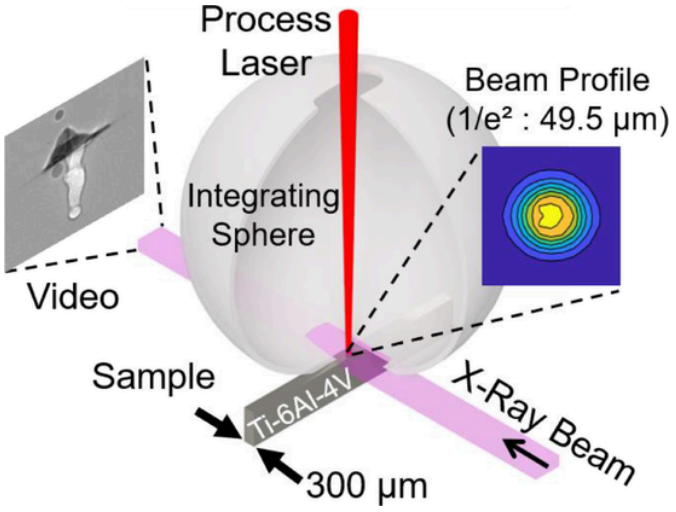


**Fig. 1.** A conceptualization of the combined integrating sphere and synchrotron x-ray imaging system. Additional information on the experimental design can be found in the appendix.

solute amount of scattered light power [21]. This procedure was repeated between laser injections so that changes to the internal surface of the sphere due to weld spatter could be accounted for.

Over the course of these experiments, the loss within the sphere changed only slightly, increasing on average by 0.6 % per laser exposure. The combined standard uncertainty in the absorption measurement was 1.3 % (coverage factor of 1). This is nearly a threefold increase in accuracy over previous efforts [21] due primarily to an improved uncertainty in laser power measurement through calibration of the laser power meter to a primary standard at the National Institute of Standards and Technology. The dynamic absorptance is determined by calculating the difference between the backscattered and input laser powers and then dividing by the input laser power. Normalizing this to 100 gives the percent absorption.

### *2.3. High-speed X-ray imaging and analysis*

All experiments were carried out at the 32-ID-B beamline of Advanced Photon Source at Argonne National Laboratory. The high-speed x-ray imaging experiments were performed similar to those of Ref. [18]. All videos in this work were captured at 50,000 frames per second with a 2.5 μs exposure time. Image analysis was performed according to the procedure in Ref. [41], which included a procedure for automatically detecting the keyhole and measuring its dimensions.

### *2.4. Process laser and chamber*

The process laser was a 1070 nm wavelength Yb-doped fiber laser with a measured spot size of 49.5 μm ± 5 μm ($1/e^2$ value). All measurements were performed with the sample at the focal plane. A *SCANLAB* intelli*SCAN*$_{de}$ 30 galvanometer scanner [40] that maintains normal incidence of the process laser beam is used for controlling the laser duration and scanning. The sample and integrating sphere apparatus were placed in an inert gas chamber with two Kapton windows that allowed for transmission of the x-ray beam. This chamber was vacuum pumped and backfilled with argon unless otherwise specified.

## 3. Results and discussion

### *3.1. Correlations of keyhole geometry and laser absorption*

During stationary and scanned laser exposures, vapor depressions were formed under various applied laser powers on Ti-6Al-4V bare plates and powders. For high-irradiance stationary exposures on bare plates, a vapor depression detection algorithm was applied to each full-field x-ray projection image. This procedure quantified the width, depth, and cross-sectional area of the vapor depression as shown in the inset of Fig. 2. For these data, a Spearman correlation coefficient was calculated to determine the degree of correlation between a cavity geometry parameter and laser absorption. A coefficient equal to 1.0 indicates perfect correlation and 0.0 means no correlation. These coefficients are plotted in Fig. 2. Recently, laser absorption and keyhole depth (measured using low-coherence interferometry) were found to be highly correlative during laser spot welding [42]. However, the results here show that absorption correlates most strongly with cavity area with depth just slightly lower, and width markedly lower. Also shown in Fig. 2 on the right ordinate is the coupling efficiency calculated as the time-integrated absorption during the entire 2.0 ms laser exposure. These data are possible through a calibration process where the absolute amount of backscattered light is determined [21]. It is worth noting that we have decreased the standard combined uncertainty of these coupling efficiency values to 1.3 %, nearly a factor of three lower than earlier work [21]. Qualitatively, the step-function behavior is similar to that found previously [21], but now x-ray images confirm in real time that this step indicates a transition from conduction mode to vapor cavity formation.

The coupling efficiency has been used to determine conditions for keyhole formation [43]. For instance, although a vapor depression is initially found at 96 W the coupling efficiency in Fig. 2 does not begin to plateau until approximately 120 W, which could be considered the onset of keyhole formation for a 2 ms laser exposure. The region between these power extremes where the average absorbed laser power sharply increases is a transition region where the vapor cavity has not yet developed into a deeper keyhole. The end of this region also marks the point at which the correlation coefficients for all geometrical parameters starts to decrease, which is presumed to be the result of increasing instability that accompanies deepening keyholes. This can be seen directly in the full high-speed x-ray videos (see Supplementary Movies 1–2). The transition regime is important for LPFB AM as one is often operating near it in order to maximize build speed while also minimizing defects associated with keyhole formation. Unfortunately, this regime is also prone to vapor cavity collapse [44] as will be explored below. Later, we will also show that even at laser powers that ensure a continuous keyhole presence, significant instability occurs which can lead to pore formation. This underscores the importance of using time-resolved laser scattering data for understanding melt pool dynamics.

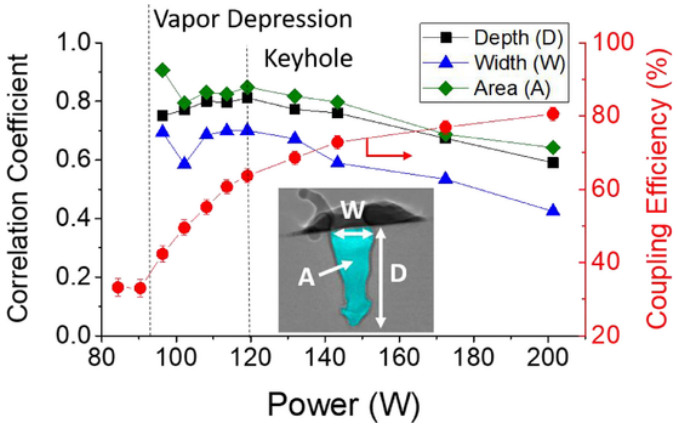


**Fig. 2.** The Spearman correlation coefficient is plotted on the left ordinate for cavity depth, area, and width (defined in inset) versus laser power for stationary laser melting of a bare Ti-6Al-4V plate. The right ordinate gives the coupling efficiency calculated by time-integrating the dynamic absorption data given by the integrating sphere. Vertical dashed lines mark the onset of vapor depression and keyhole formation.

### 3.2. Vapor cavity collapse

For LPBF, vapor cavity stability is generally considered a prerequisite for achieving a high-quality final part. Achieving the correct balance of forces for metastability can be challenging though as slight changes to the laser processing conditions (i.e. scan speed, laser power, beam size, etc.) can have drastic effects. Here, for the purpose of study, instability is created by increasing the amount of oxygen in the build chamber during a stationary laser exposure. Oxygen is a surface active element that alters the surface tension [45] and has been shown to contribute to defect formation in LPBF [46].

In Fig. 3, the top and middle rows were obtained with 90.0 W of incident laser power for 5.0 ms on a bare Ti-6Al-4V plate in an argon atmosphere and in air, respectively. Since the x-ray imaging is under-sampled compared to the light scattering experiments (50 kHz versus 25 MHz), synchronization of the two data sets is achieved by an electronic timing signal that allows for the temporal location of each individual video frame to be determined. These are marked by blue squares in Fig. 3(a), (d), and (g). The absorption data in Fig. 3(a) shows a sharp transition from an average of 33% absorption in the first 2.4 ms to 66% for the remainder of the total 5 ms laser exposure – a doubling of the amount of absorbed laser power. From high-speed x-ray images, this rise corresponds to the formation of a vapor cavity with representative images given in Fig. 3(b) and (c). In air however, keyhole formation becomes more erratic. In an inert atmosphere (Ar), the keyhole consistently formed at 2.4 ms (repeated 5 times), whereas in air keyholing always began sooner but with a varied formation time between 0.8 and 1.3 ms. Fig. 3(d), for example, shows two distinct keyhole regions occurring in a single 5.0 ms laser exposure. The consistently faster keyhole initiation could be the result of increased absorption due to oxide formation at the surface [47].

The presence of powder represents another contributor to cavity instability as compared to bare plate. Fig. 3(g)–(i) shows results from a stationary laser exposure (114 W, 2.0 ms) on a thin Ti-6Al-4V powder layer (100 μm thickness) on a solid metal substrate in an Ar environment. These data do not reveal the clean, step-function behavior seen in Fig. 3(a). Instead, an initially high absorption (> 50 %), typical for powder surfaces [22], gives way to brief periods of cavity formation identified by x-ray imaging (shaded regions in Fig. 3(g)). An x-ray image from this region is shown in Fig. 3(i). Here, there is an increase in absorption from 42 % to 66 %. In terms of scattered laser light intensity, the formation of a keyhole reduces the measured signal by 41 % for a powder bed surface and by about 50 % on a bare plate. These dramatic changes are easily resolvable by ISR. And, since only the relative change in scattered laser intensity is necessary for detecting these cavity formation and collapse events, one does not need to frequently perform the sophisticated sensor calibration making this technique more practical as a real-time monitoring tool for LPBF AM.

### 3.3. Real-time detection of keyhole-induced pore formation mechanism

In addition to observing vapor depression formation and collapse, more subtle changes in backscattered light can reveal important dynamics during strong keyhole formation. At relatively high applied laser powers, the average coupling efficiency plateaus at over 70% for Ti-6Al-4V bare plate, which is attributed to deep keyhole formation (see Fig. 2). However, rapid variations in the absorption signal and supporting x-ray images indicate that during strong keyhole forming conditions (high laser power), instability can lead to pore formation. Fig. 4(a), shows absorption data from a stationary laser exposure of 2 ms at 201 W on bare plate. The sharp rise in absorption at 35 μs results from strong keyhole formation due to the relatively high irradiance of 2.6 MW/cm$^2$. Once the keyhole is formed, the average absorp-

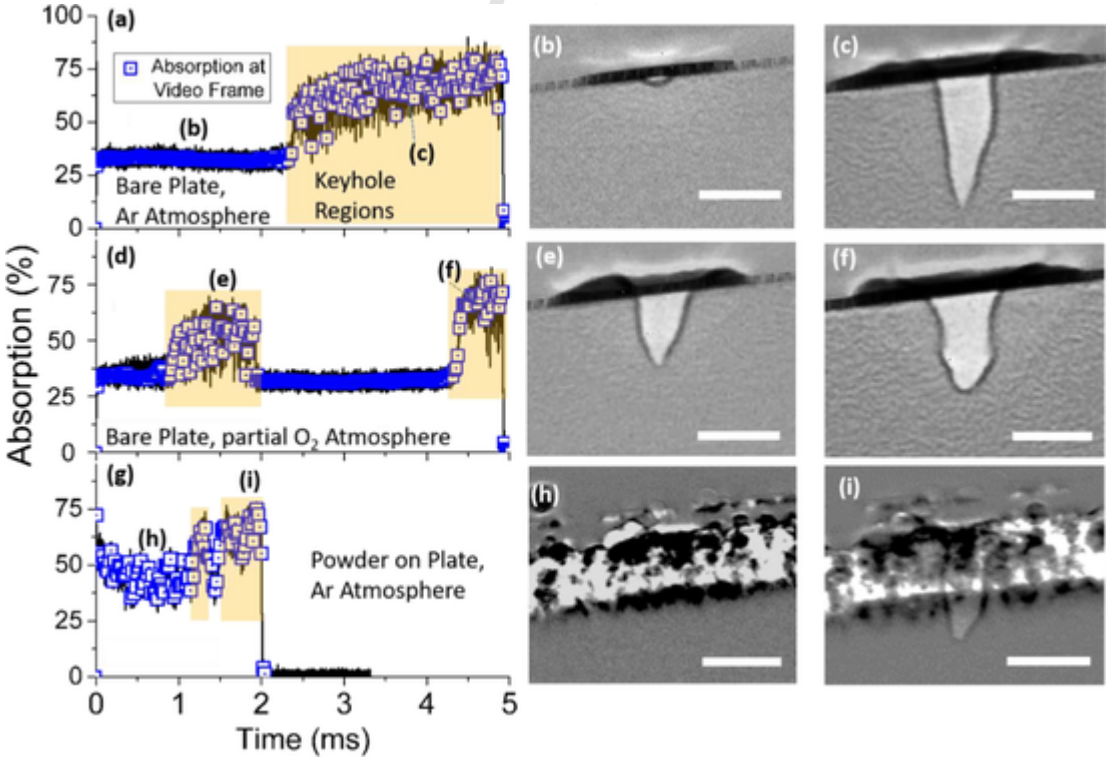


**Fig. 3.** Simultaneous ISR and x-ray imaging data revealing stationary laser beam (90 W, 5 ms) melting of a bare Ti-6Al-4V plate in argon (a) and in air (d). Data is also shown for a stationary beam (114 W, 2 ms) incident on a Ti-6Al-4V powder bed sample in argon (g). The ISR and x-ray imaging data were synchronized so that the under-sampled location of each x-ray image could be identified (blue squares). Selected x-ray images are given with their temporal location indicated by the letters in (a), (d), and (g). All scale bars are 100 μm. (For interpretation of the references to color in this figure legend, the reader is referred to the web version of this article.)

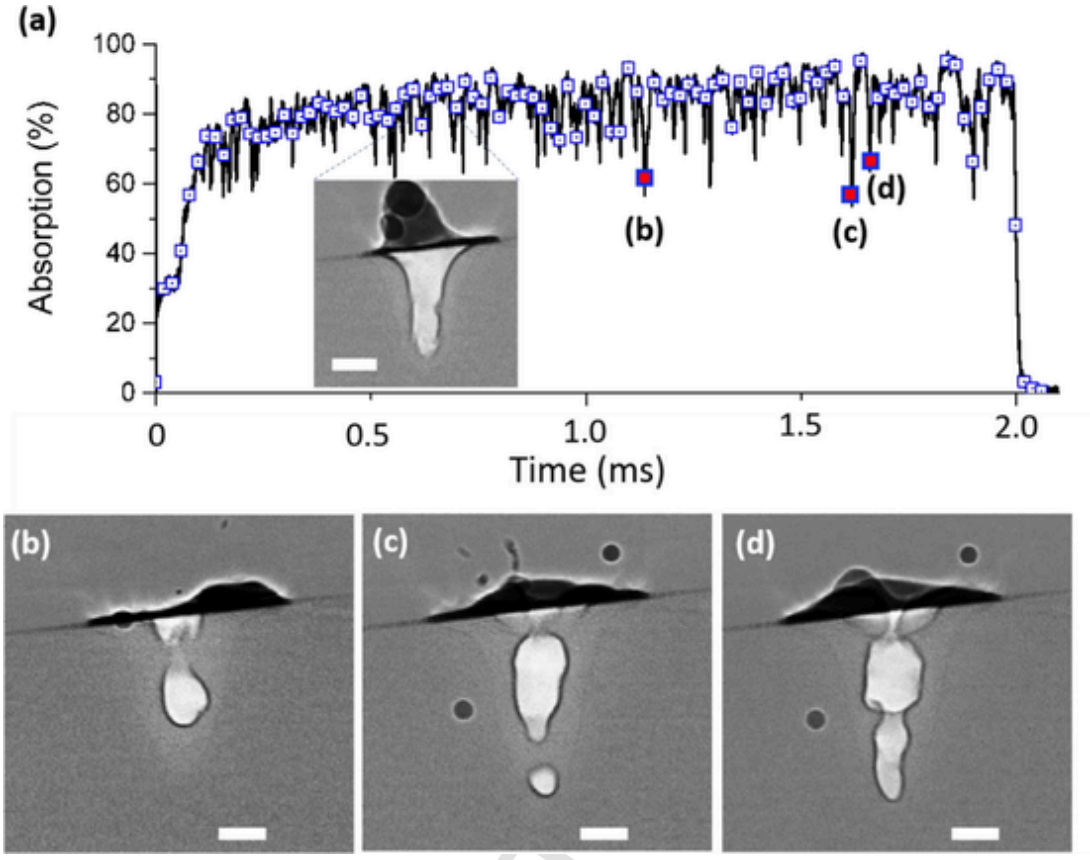


**Fig. 4.** Rapid instability demonstrated during a stationary laser exposure (201 W, 2 ms) on a Ti-6Al-4V bare plate. (a) The blue squares indicate the location of x-ray video frames. Specific x-ray images are given in (b), (c), and (d) with their locations shown with letters in (a). The scale bars are 100 μm.

tion is 84 % with a standard deviation of 6.6%. One can also notice several brief reductions in absorption lasting less than 10 μs each, with examples identified by letters (b)–(d). The average absorption during these events is 58.5%, well below the overall average.

The image inset in Fig. 4a shows a representative x-ray image when the absorption is near the keyhole average (84%). In this dataset, three of the events corresponding to the rapid drops in absorption were captured in the x-ray images shown in Fig. 4(b)–(d). At these points in time, the keyhole opening has severely narrowed allowing significantly less light to enter. From an understanding of cavity absorption involving multiple reflections, we conclude that these sudden collapses are causal to the drastic, momentary reduction of absorption. This is reinforced by the fact that frames before and after show relatively open keyholes like that shown in the inset of Fig. 4(a) (See Supplementary Movie 3). The appearance and timescale of these features are consistent with dynamics predicted to cause keyhole-induced porosity and defects [11,14,48]. Their correlation with momentary, yet drastic, reductions in laser absorption means that by monitoring the integrated backscattered laser light, one is able to observe this behavior in real-time in the hopes of developing feed-forward control system for reducing porosity.

### *3.4. Scanned laser vapor cavity dynamics*

The results presented thus far have been for a stationary laser, which although instructive for understanding the fundamentals of vapor depression dynamics, is too far from realistic LPBF conditions to be directly applicable. Therefore, scanned laser experiments were performed to investigate vapor depression stability on bare plate and metal powder under nominally consistent keyhole conditions. These conditions were approximated from scaling laws for keyhole depth as a function of laser scan speed, beam diameter, and material properties on a bare metal plate [44]. These laws define a threshold power for keyhole formation defined as a vapor depression with aspect ratio equal to 1 (see Eq. (11) in Ref. [44]), which for the scan speed (0.7 m/s) and spot diameter (49.5 μm) used here should be roughly 100 W. The scaling law also stipulate that a laser power of at least 1.7 times this value ensures a consistent keyhole not prone to collapse. Fig. 5 shows results for the scanned laser melting of Ti-6Al-4V plate and powder bed samples with 0.7 m/s scan speed and 201 W power. Example video frames are shown in Fig. 5(b) and (c) with their approximate locations indicated in Fig. 5(a) (see also Supplementary Movie 4).

The data in Fig. 5(a)–(c) reveal an interesting phenomenon. Although obtained under constant scan velocity where a "sky-write" scan strategy is employed to ensure a constant laser dwell time, the x-ray images show an initial keyhole with a significantly higher aspect ratio than that obtained at later times. Under these processing conditions, a steady state is achieved after about 400 μs of laser exposure. Qualitatively, similar behavior is found when a 100 μm thick powder bed is prepared on a solid substrate as seen in Fig. 5(d)–(f) (see also Supplementary Movie 5). A subtle difference is that the initial absorption is higher in powder than a solid surface due to increased light trapping from a porous surface [49]. Variations in the powder packing fraction can affect the initial absorption [22,50], but only for the brief period of time before the particles melt ($< 20$ μs here). To estimate this affect, a 20% change in the initial powder absorption from 55% to 44% would amount to only a 0.14% reduction in total energy absorbed over the 2.0 ms laser exposure in Fig. 5(d). Therefore, this would seem to be too small to have much of an affect on melt pool dynamics much later in the exposure.

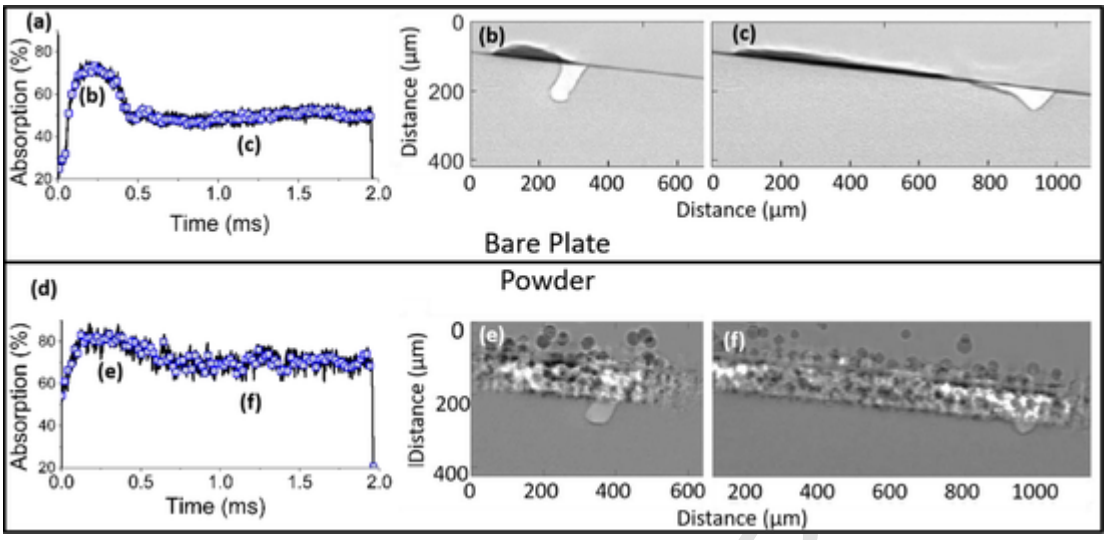


**Fig. 5.** Laser absorption and cross-sectional x-ray imaging for bare metal (top row) and a 100 μm thick powder bed sample of Ti-6Al-4V (bottom). The blue squares indicate the specific temporal location of high-speed x-ray frames. The location of the frames given in (b), (c), (e), and (f) are marked by letters in (a) and (d). The laser spot size is 49.5 μm, power is 201 W, and scan speed is 0.7 m/s.

The transition from an initially deep keyhole to a shallower one is primarily the result of metal vaporization and fluid dynamics. This observation occurs at early timescales where vaporization dominates before the steady-state convective fluid flow is established. The initial keyhole forms very rapidly ($< 50$ μs), and thus the vaporization-induced recoil force is highly localized. Once the keyhole forms, the scanning laser is primarily incident to the front keyhole wall [44] making it the hottest surface with the strongest vaporization. The metal vapor is released normal to this surface, but at early times is deflected upwards by the rear keyhole wall [51] consequently driving the keyhole deeper. The vapor creates a fricative force against the rear keyhole wall that eventually acts to move molten metal away. Simultaneously, a strong Marangoni convection develops near the rear keyhole wall that moves the hotter molten metal towards the colder region, in the direction opposite to the laser scan [11,52]. In time, these effects act together to lower the height of the rear keyhole rim. Once this occurs, the vapor is no longer deflected straight upward and the keyhole depth is reduced. As the keyhole opens and shallows, fewer multiple reflections occur which lowers the total energy absorbed.

This sudden change in keyhole aspect ratio can cause the collapse of keyhole walls, which must be mitigated to achieve a high quality as-built part [48]. As we find that this change occurs shortly after laser illumination begins ($< 1$ ms), scan strategies such as “island” and “sky-write” techniques, which require thousands of laser starts and stops throughout a build, would be most significantly affected. A drastic keyhole morphological change is also seen in LPBF as a scanned laser beam turns a corner, although in this case, due to a change in laser dwell time as the scan speed slows and then accelerates creating so-called turnaround pores [48]. Based on our findings, this sudden change in keyhole aspect ratio should also be detectable by a total backscattered light detection system allowing for the possibility of real-time detection.

### *3.5. Dynamic keyhole depth and absorption examined with a normalized enthalpy model*

The data presented thus far demonstrate the strong connection between relative changes to the backscattered light and changes in the vapor depression aspect ratio. However, since our ISR was calibrated to calculate absolute absorptance, a more quantitative assessment is also possible. Recently, it has been demonstrated that the keyhole depth can be estimated from the normalized enthalpy of the melt pool system [6,24,53]. Rubenchik et al. show that the keyhole depth, $d$, normalized by the thermal diffusion length, $L_{th}$, is linearly dependent on the total enthalpy normalized by the enthalpy of melting, $H_m$ [53]. This model has the intuitive interpretation that additional absorbed energy in excess of that required for melting is responsible for determining the melt pool depth. This is a simplified model as it does not consider convective or evaporative energy losses, yet it has been shown to be universally true for a wide range of materials including Ti-6Al-4V, stainless steel, and nickel-based superalloy Inconel 625 [24,53]. In our experiments, we test the validity of this model during a single laser exposure by calculating the normalized enthalpy, $\beta$, as [24]

$$\beta = \frac{A\,P}{\pi H_m \sqrt{Dua^3}} \tag{1}$$

where $A$ is the laser absorptance, $P$ is the laser power, $D$ is the thermal diffusivity, $u$ is the scan speed, and $a$ is the beam radius. The time dependence of $\beta$ is due to the temporal behavior of $A$, which is measured directly with ISR.

Fig. 6 shows the normalized keyhole depth ($d/L_{th}$) versus normalized enthalpy for the scan in Fig. 5(a)–(c). Thermal properties of $L_{th}$, $H_m$, $D$ for Ti-6Al-4V are taken from Ref. [24] and references therein. In previous studies using this model, the laser absorption was treated as a constant and the linear relationship was demonstrated for a range of applied laser powers and material properties necessitating dozens of separate experiments. Here, however, the simultaneously measured, real-time absorptance and keyhole depth during a constant laser irradiation are compared, and interestingly, a linear dependence is also found. The bare plate data (black, closed squares) shows a strong linear relationship with a Pearson correlation coefficient of 0.98. The powder data (red, open squares) have more noise, but is still reasonably linear with a correlation coefficient of 0.70. A linear fit of the bare plate data reveals a slope of 0.42, which is close to the value of 0.60 found by Ye et al. [24] Potential reasons for the discrepancy are that Ye et al. calculated $\beta$ from the time-averaged absorption as opposed to a real-time value, and they determined the depth from cross-sections of the solidified melt pools instead of the keyhole bottom as done here. As for the powder sample, the slope determined from the linear fit is 0.31 (red line), whose deviation from the bare plate could be due to the differences in thermophysical property values between plate and powder. These experiments were repeated but at a slightly higher laser power

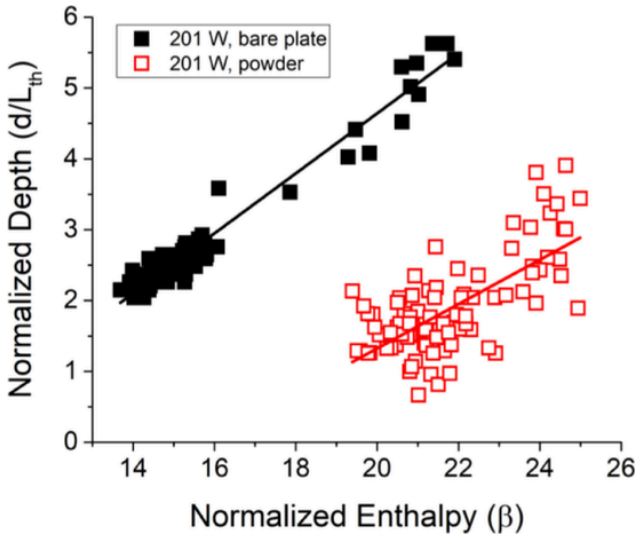


**Fig. 6.** Normalized keyhole depth versus the normalized enthalpy that is a function of the simultaneously measured absorptance during the scanned laser melting (201 W, 0.7 m/s) of Ti-6Al-4V plotted. The solid squares are from a bare plate sample and the open squares are from a powder bed sample. The solid lines are linear fits to the data.

(261 W) with results presented in the Supplementary Fig. S1. At this power, similar behavior is found, albeit with slightly more noise due to increased keyhole instability.

The observation that the normalized enthalpy model is applicable during a single laser exposure at a time resolution of 20 μs is important for understanding the basic physics of the LPBF process, but it also leads to a practical application. Under transient LPBF conditions where the keyhole rapidly changes, if one knows the instantaneous absorbed laser power the keyhole depth can be estimated using this model. These results demonstrate the feasibility of leveraging calibrated backscattered laser light detection for real-time monitoring of this critical dimension under constant laser settings. This is critical for assuring the reliability of as-built complex structures using LPBF, in which keyhole morphology and laser absorption can be substantially different across the build such as at the end of tracks, thin walls, edges, corners, and laser turn points.

## 4. Conclusions

This work quantifies the relationship between laser power absorption and melt pool cavity geometry at a level that has not been previously available. Prior measurements of laser absorption have either been time-averaged [43,54], and thus incapable of real-time correlation, or time-resolved but only related to solidified melt pools characterized *ex situ* [21]. The closest to date has been Allen et al. who combined ISR and inline coherent imaging but were limited to stationary laser measurements on solid samples and only one-dimension geometry data [42,55]. Therefore, this work represents a significant advancement that allows for testing the fundamental relationship like that expressed in the normalized enthalpy model and as a resource for validating multiphysics simulations.

Qualitatively, the correlation of sharp changes to the backscattered light signal with pore-defect-creating mechanisms demonstrates the utility of this technique for a simple, real-time, *in situ* process monitor. Recently, researchers put forth process recommendations for reducing porosity related to changes in keyhole aspect ratio [48] and keyhole instability [14]. However, the diagnostic techniques used in these studies cannot be readily incorporated into a manufacturing environment. Our results demonstrate that measurements of total backscattered light are not only capable of real-time detection of keyhole collapses, aspect ratio deviations, and instabilities, but do so in a manner that is readily applicable to industrial laser processes.

## CRediT authorship contribution statement

**Brian J. Simonds:** Conceptualization, Formal analysis, Investigation, Writing – original draft, Supervision. **Jack Tanner:** Investigation, Visualization. **Alexandra Artusio-Glimpse:** Software. **Paul A. Williams:** Investigation, Writing – review & editing. **Niranjan Parab:** Investigation. **Cang Zhao:** Investigation. **Tao Sun:** Investigation, Writing – review & editing, Resources.

## Declaration of Competing Interest

The authors declare that they have no known competing financial interests or personal relationships that could have appeared to influence the work reported in this paper.

## Data availability statement

The authors will make data available upon reasonable request.

## Acknowledgments

This research used resources of the Advanced Photon Source, a U.S. Department of Energy (DOE) Office of Science User Facility operated for the DOE Office of Science by Argonne National Laboratory under Contract No. DE-AC02-06CH11357. The authors also thank Lyle Levine and Nick Derimow for useful comments and discussion on this manuscript.

## Supplementary materials

Supplementary material associated with this article can be found, in the online version, at doi:10.1016/j.apmt.2021.101049.

## References

[1] M.C. Fery, On the approximation of black bodies which are employed as receivers, C. R. 148 (1909) 777–780.
[2] A. Gouffe, Corrections d'ouverture des corps noirs artificiels compte tenu des diffusions multiples internes, Rev. Opt. 24 (1945) 1–10.
[3] E.M. Sparrow, V.K. Jonsson, Radiant emission characteristics of diffuse conical cavities, J. Opt. Soc. Am. 53 (1963) 816–821.
[4] E.D. West, L.B. Schmidt, Spectral-absorptance measurements for laser calorimetry, J. Opt. Soc. Am. 65 (1975) 573–578, doi:10.1364/JOSA.65.000573.
[5] D.T. Swift-Hook, A.E.F. Gick, Penetration welding with lasers, Weld. J. 52 (1973) 492s–499s. https://unicorn.dmz.cranfield.ac.uk/uhtbin/cgisirsi/?ps=MHwR2FMU8e/CRANFIELD/141340320/9.
[6] W.E. King, H.D. Barth, V.M. Castillo, G.F. Gallegos, J.W. Gibbs, D.E. Hahn, C. Kamath, A.M. Rubenchik, Observation of keyhole-mode laser melting in laser powder-bed fusion additive manufacturing, J. Mater. Process. Technol. 214 (2014) 2915–2925.
[7] R. Cunningham, C. Zhao, N. Parab, C. Kantzos, J. Pauza, K. Fezzaa, T. Sun, A.D. Rollett, Keyhole threshold and morphology in laser melting revealed by ultrahigh-speed x-ray imaging, Science (80-.) 363 (2019) 849–852, doi:10.1126/science.aav4687.
[8] S.C. Wang, P.S. Wei, Energy-Beam redistribution and absorption in a drilling or welding cavity, Metall. Trans. B 23 (1992) 505–511, doi:10.1007/BF02649669.
[9] P. Solana, G. Negro, A study of the effect of multiple reflections on the shape of the keyhole in the laser processing of materials, J. Phys. D Appl. Phys. 30 (1997) 3216–3222, doi:10.1088/0022-3727/30/23/006.
[10] C.Y. Ho, P.S. Wei, Energy absorption in a conical cavity truncated by spherical cap subject to a focused high-intensity beam, Int. J. Heat Mass Transf. 40 (1997) 1895–1905, doi:10.1016/S0017-9310(96)00223-2.
[11] N. Kouraytem, X. Li, R. Cunningham, C. Zhao, N. Parab, T. Sun, A.D. Rollett, A.D. Spear, W. Tan, Effect of laser-matter interaction on molten pool flow and keyhole dynamics, Phys. Rev. Appl. 11 (2019) 064054, doi:10.1103/PhysRevApplied.11.064054.
[12] S.A. Khairallah, A.A. Martin, J.R.I. Lee, G. Guss, N.P. Calta, J.A. Hammons, M.H. Nielsen, K. Chaput, E. Schwalbach, M.N. Shah, M.G. Chapman, T.M. Willey, A.M. Rubenchik, A.T. Anderson, Y.M. Wang, M.J. Matthews, W.E. King, Controlling interdependent meso-nanosecond dynamics and defect generation in metal 3D printing, Science (80-.) 368 (2020) 660–665.
[13] J. Lind, F. Fetzer, D. Blazquez-sanchez, J. Weidensdörfer, R. Weber, J. Lind, Geometry and absorptance of the cutting fronts during laser beam cutting

Geometry and absorptance of the cutting fronts during laser beam cutting, J. Laser Appl. 032 (2020) 1–5, doi:10.2351/7.0000024.
[14] M. Bayat, A. Thanki, S. Mohanty, A. Witvrouw, S. Yang, J. Thorborg, N.S. Tiedje, J.H. Hattel, Keyhole-induced porosities in laser-based powder bed fusion (L-PBF) of Ti6Al4V: high-fidelity modelling and experimental validation, Addit. Manuf. 30 (2019) 100835, doi:10.1016/j.addma.2019.100835.
[15] L. Aucott, H. Dong, W. Mirihanage, R. Atwood, A. Kidess, S. Gao, S. Wen, J. Marsden, S. Feng, M. Tong, T. Connolley, M. Drakopoulos, C.R. Kleijn, I.M. Richardson, D.J. Browne, R.H. Mathiesen, H.V. Atkinson, Revealing internal flow behaviour in arc welding and additive manufacturing of metals, Nat. Commun. 9 (2018) 1–7, doi:10.1038/s41467-018-07900-9.
[16] F. Fetzer, C. Hagenlocher, R. Weber, T. Graf, Geometry and stability of the capillary during deep-penetration laser welding of AlMgSi at high feed rates, Opt. Laser Technol. 133 (2020) 106562.
[17] C. Zhao, K. Fezzaa, R.W. Cunningham, H. Wen, F. De Carlo, L. Chen, A.D. Rollett, T. Sun, Real-time monitoring of laser powder bed fusion process using high-speed X-ray imaging and diffraction, Sci. Rep. 7 (2017) 3602, doi:10.1038/s41598-017-03761-2.
[18] N.D. Parab, L.I. Escano, K. Fezzaa, W. Everhart, A.D. Rollett, L. Chen, T. Sun, Ultrafast X-ray imaging of laser – metal additive manufacturing processes, J. Synchrotron Radiat. 25 (2018) 1467–1477, doi:10.1107/S1600577518009554.
[19] C. Sainte-Catherine, M. Jeandin, D. Kechemair, J.-P. Ricaud, L. Sabatier, Study of dynamic absorptivity at 10.6 μm ($CO_2$) and 1.06 μm (Nd-YAG) wavelengths as a function of temperature, J. Phys. IV 1 (1991) 151–157, doi:10.1051/jp4:1991741>.
[20] J.T. Norris, C.V Robino, M.J. Perricone, D.A. Hirschfeld, Development of a time-resolved energy absorption measurement technique for laser beam spot welds, Weld. J. 89 (2010) 75 s-81-s.
[21] B.J. Simonds, J. Sowards, J. Hadler, E. Pfeif, B. Wilthan, J. Tanner, P. Williams, J. Lehman, Time-resolved absorptance and melt pool dynamics during intense laser irradiation of metal, Phys. Rev. Appl. 10 (2018) –14 044061, doi:10.1103/PhysRevApplied.10.044061.
[22] B.J. Simonds, E.J. Garboczi, T.A. Palmer, P.A. Williams, Dynamic laser absorptance measured in a geometrically characterized stainless-steel powder layer, Phys. Rev. Appl. 13 (2020) 024057.
[23] W. Tan, S.B. Neil, C.S. Yung, Investigation of keyhole plume and molten pool based on a three-dimensional dynamic model with sharp interface formulation, J. Phys. D Appl. Phys. 46 (2013) 55501, doi:10.1088/0022-3727/46/5/055501.
[24] J. Ye, S.A. Khairallah, A.M. Rubenchik, M.F. Crumb, G. Guss, J. Belak, M.J. Matthews, Energy coupling mechanisms and scaling behavior associated with laser powder bed fusion additive manufacturing, Adv. Eng. Mater. 1900185 (2019) 1900185, doi:10.1002/adem.201900185.
[25] S.K. Everton, M. Hirsch, P. Stravroulakis, R.K. Leach, Review of in situ process monitoring and in situ metrology for metal additive manufacturing, Mater. Des. 95 (2016) 431–445, doi:10.1016/j.matdes.2016.01.099.
[26] T.G. Spears, S.A. Gold, In-process sensing in selective laser melting (SLM) additive manufacturing, Integr. Mater. Manuf. Innov. 5 (2016) 16–40, doi:10.1186/s40192-016-0045-4.
[27] G. Tapia, A. Elwany, A review on process monitoring and control in metal-based additive manufacturing, J. Manuf. Sci. Eng. Trans. ASME (2014) 136, doi:10.1115/1.4028540.
[28] S. Clijsters, T. Craeghs, S. Buls, K. Kempen, J.P. Kruth, In situ quality control of the selective laser melting process using a high-speed, real-time melt pool monitoring system, Int. J. Adv. Manuf. Technol. 75 (2014) 1089–1101, doi:10.1007/s00170-014-6214-8.
[29] J.A. Mitchell, T.A. Ivanoff, D. Dagel, J.D. Madison, B. Jared, Linking pyrometry to porosity in additively manufactured metals, Addit. Manuf. (2020) 31, doi:10.1016/j.addma.2019.100946.
[30] C. Zhao, Q. Guo, X. Li, N. Parab, K. Fezzaa, W. Tan, L. Chen, T. Sun, Bulk-explosion-induced metal spattering during laser processing, Phys. Rev. X 9 (2019) 021052, doi:10.1103/PhysRevX.9.021052.
[31] S.M.H. Hojjatzadeh, N.D. Parab, Q. Guo, M. Qu, L. Xiong, C. Zhao, L.I. Escano, K. Fezzaa, W. Everhart, T. Sun, L. Chen, International journal of machine tools and manufacture direct observation of pore formation mechanisms during LPBF additive manufacturing process and high energy density laser welding, Int. J. Mach. Tools Manuf. 153 (2020) 103555, doi:10.1016/j.ijmachtools.2020.103555.
[32] S. Shevchik, T. Le-quang, B. Meylan, F.V. Farahani, K. Wasmer, Supervised deep learning for real- time quality monitoring of laser welding with X-ray radiographic guidance, Sci. Rep. 10 (2020) 3389.
[33] A.F.H. Kaplan, P. Norman, I. Eriksson, Analysis of the keyhole and weld pool dynamics by imaging evaluation and photodiode monitoring, Proceedings of the LAMP2009, 2009, pp. 1–6. http://pure.ltu.se/portal/files/3434918/Kaplan_AFH_LAMP_2009_manuscript.pdf.
[34] J.-B. Forien, N.P. Calta, P.J. DePond, G.M. Guss, T.T. Roehling, M.J. Matthews, Detecting keyhole pore defects and monitoring process signatures during laser powder bed fusion: a correlation between in situ pyrometry and ex situ X-ray radiography, Addit. Manuf. (2020) 101336, doi:10.1016/j.addma.2020.101336.
[35] A.R. Nassar, T.J. Spurgeon, E.E. Reutzel, Sensing defects during directed-energy additive manufacturing of metal parts using optical emissions spectroscopy, Solid Free Fabr. Proc. (2014) 278–287, doi:10.1017/CBO9781107415324.004.
[36] B.J. Simonds, P. Williams, J. Lehman, Time-resolved detection of vaporization during laser metal processing with laser-induced fluorescence, Proc. CIRP 74 (2018) 628–631, doi:10.1016/j.procir.2018.08.072.
[37] U.M. Dilberoglu, B. Gharehpapagh, U. Yaman, M. Dolen, The role of additive manufacturing in the era of industry 4.0, Proc. Manuf. 11 (2017) 545–554, doi:10.1016/j.promfg.2017.07.148.
[38] T. Mukherjee, T. DebRoy, A digital twin for rapid qualification of 3D printed metallic components, Appl. Mater. Today 14 (2019) 59–65, doi:10.1016/j.apmt.2018.11.003.
[39] S. 654b, Titanium Alloy, Al-V, (n.d.).
[40] Certain commercial equipment, software, and/or materials are identified in this paper in order to adequately specify the experimental procedure. In no case does such identification imply recommendation or endorsement by the National Institute of Standards., (n.d.).
[41] B.J. Simonds, J.R. Tanner, A. Artusio-Glimpse, P.A. Williams, N.D. Parab, C. Zhao, T. Sun, Simultaneous high-speed x-ray transmission imaging and absolute dynamic absorptance measurements during high-power laser-metal processing, Proc. CIRP 94 (2020) 775–779.
[42] T.R. Allen, W. Huang, J. Tanner, W. Tan, J.M. Fraser, B.J. Simonds, Energy-coupling mechanisms revealed through simultaneous keyhole depth and absorptance measurements during laser-metal processing, Phys. Rev. Appl. 13 (2020) 064070.
[43] J. Trapp, A.M. Rubenchik, G. Guss, M.J. Matthews, In situ absorptivity measurements of metallic powders during laser powder-bed fusion additive manufacturing, Appl. Mater. Today 9 (2017) 341–349, doi:10.1016/j.apmt.2017.08.006.
[44] R. Fabbro, Depth dependence and keyhole stability at threshold, for different laser welding regimes, Appl. Sci. 10 (2020) 1–22, doi:10.3390/app10041487.
[45] S. Lu, H. Fujii, K. Nogi, Sensitivity of Marangoni convection and weld shape variations to welding parameters in $O_2$-Ar shielded GTA welding, Scr. Mater. 51 (2004) 271–277, doi:10.1016/j.scriptamat.2004.03.004.
[46] C.L. Alex Leung, S. Marussi, M. Towrie, R.C. Atwood, P.J. Withers, P.D. Lee, The effect of powder oxidation on defect formation in laser additive manufacturing, Acta Mater. 166 (2019) 294–305, doi:10.1016/j.actamat.2018.12.027.
[47] H. Kwon, W.K. Baek, M.S. Kim, W.S. Shin, J.J. Yoh, Temperature-dependent absorptance of painted aluminum, stainless steel 304, and titanium for 1.07 um and 10.6 um laser beams, Opt. Lasers Eng. 50 (2012) 114–121, doi:10.1016/j.optlaseng.2011.10.001.
[48] A.A. Martin, N.P. Calta, S.A. Khairallah, J. Wang, P.J. Depond, A.Y. Fong, V. Thampy, G.M. Guss, A.M. Kiss, K.H. Stone, C.J. Tassone, J.N. Weker, M.F. Toney, T. van Buuren, M.J. Matthews, Dynamics of pore formation during laser powder bed fusion additive manufacturing, Nat. Commun. 10 (2019) 1987, doi:10.1038/s41467-019-10009-2.
[49] A.V. Gusarov, I. Yadroitsev, P. Bertrand, I. Smurov, Model of radiation and heat transfer in laser-powder interaction zone at selective laser melting, J. Heat Transf. 131 (2009) 072101, doi:10.1115/1.3109245.
[50] A.V. Gusarov, J.P. Kruth, Modelling of radiation transfer in metallic powders at laser treatment, Int. J. Heat Mass Transf. 48 (2005) 3423–3434, doi:10.1016/j.ijheatmasstransfer.2005.01.044.
[51] R. Fabbro, S. Slimani, I. Doudet, F. Coste, F. Briand, Experimental study of the dynamical coupling between the induced vapour plume and the melt pool for Nd-Yag CW laser welding, J. Phys. D Appl. Phys. 39 (2006) 394–400, doi:10.1088/0022-3727/39/2/023.
[52] R. Fabbro, Melt pool and keyhole behaviour analysis for deep penetration laser welding, J. Phys. D Appl. Phys. (2010) 43, doi:10.1088/0022-3727/43/44/445501.
[53] A.M. Rubenchik, W.E. King, S.S. Wu, Scaling laws for the additive manufacturing, J. Mater. Process. Technol. 257 (2018) 234–243, doi:10.1016/j.jmatprotec.2018.02.034.
[54] P.W. Fuerschbach, Measurement and prediction of efficiency in laser beam energy transfer welding, Weld. J. 75 (1996) 24s–34s.
[55] T.R. Allen, B.J. Simonds, J.R. Tanner, J.M. Fraser, Simultaneous in operando monitoring of keyhole depth and absorptance in laser processing of AISI 316 stainless steel at 200 kHz, Proc. CIRP 94 (2020) 419–424, doi:10.1016/j.procir.2020.09.157.
[56] Brandon Lane, Ivan Zhirnov, Sergey Mekjontsev, Steven Grantham, Richard Ricker, Santosh Rauniyar, Kevin Chou, Transient Laser Energy Absorption, Co-axial Melt Pool Monitoring, and Relationship to Melt Pool Morphology, Additive Manufacturing 36 (101504) (2020) 1–13.